Lateral line profiles in fast-atom diffraction at surfaces

Peng Pan [1], Carina Kanitz [1,2] Maxime Debiossac [1], Alex Le-Guen [1], Jaafar Najafi Rad [1], and Philippe Roncin [1]

[1]*Université Paris-Saclay, CNRS, Institut des Sciences Moléculaires d'Orsay (ISMO), Orsay, France*

[2]*German Aerospace Center (DLR), Institute of Quantum Technologies, Wilhelm-Runge-Straße 10, Ulm, Germany*

Grazing incidence fast-atom diffraction (GIFAD) uses keV atoms to probe the topmost layer of crystalline surfaces. The atoms are scattered by the potential energy landscape of the surface onto elastic diffraction spots located at the Bragg angles and on the Laue circle. However, atoms transfer a significant momentum to the surface, giving rise to possible phonon excitation. This causes the inelastic intensity to spread above and below the circle along the direction of the surface normal. The relative intensity of the elastic contribution is well fitted by the Debye-Waller model adapted to GIFAD, but the composite azimuthal line profile governing the ability to resolve diffraction spots has not been investigated in detail. The paper reports a series of diffraction measurements of helium on a LiF(001) surface revealing marked differences in the polar (θ) and lateral (ϕ) inelastic profiles but also similarities in the evolution of their line widths σ_θ and σ_ϕ. We observe two regimes: When elastic diffraction is significant, the Laue circle appears as a reference for inelastic diffraction; the azimuthal inelastic line shape is an exponential decay and its width increases almost linearly as the scattering angle deviates from the specular condition. When elastic diffraction weakens, the inelastic line shape evolves towards a Gaussian and its width is no longer minimum on the Laue circle. As a possible difference with x ray, neutrons, and electrons, the in-plane motion of surface atoms may not be the dominant cause of the broadening of the lateral profile in GIFAD.

I. INTRODUCTION

Grazing incidence fast-atom diffraction at crystal surfaces (GIFAD or FAD) uses atoms in the keV energy range at incidence angles around $1°$, so that the largest component of the velocity or wave vector is parallel to the surface (see Fig. 1 and Table IV). When the surface coherence permits, a rich diffraction pattern containing up to a hundred well-resolved diffraction orders can be obtained [1] on a position-sensitive detector [2]. GIFAD is fast enough to produce several images per second allowing online tracking of thin film growth in UHV conditions [3]. Both detection and collection efficiencies are close to one because the large projectile kinetic energy gives rise to a small value of the Bragg angle $\phi_B \simeq G_\perp/k_\parallel$ (see Table I) where $G_\perp$ is the reciprocal lattice vector and $k_\parallel$ the projectile wave vector along the probed crystal axis.

The drawback is that the diffraction spots are close to each other requiring an angular resolution of a few mdeg. In addition, the large mass of the projectile gives rise to important inelastic effects so that the elastic diffraction peaks are accompanied by an inelastic component. The resulting azimuthal line shape is therefore composite but has never been addressed as such. This is in part because the elastic diffraction was not observed until Refs. [1,4–7], probably due to a limited surface coherence in earlier work. The investigation of the azimuthal (lateral) line shape and in particular the inelastic component is the main focus of the present paper. As with all diffraction techniques, the location of the diffraction spot only indicates the surface periodicity while the detailed information on what constitutes the unit cell is associated with the relative intensity I_m of the elastic diffraction orders ($\Sigma_m I_m = 1$). An accurate

comparison with theory requires a careful evaluation of intensities taking into account the spot profile contaminated by the inelastic profile and the possible overlap of adjacent diffraction orders. In addition, a better description of the inelastic profile might provide a better understanding of the inelastic processes at play.

The elastic profile is represented by a delta function $\delta(x)$ with a weight a and the inelastic one by a function $f(\phi)$ listed in Table II and a weight $(1 - a)$. The sum is then convoluted (noted *) by a Gaussian of width σ_b fitted to the beam profile measured immediately before or after the experiment. The composite profile, noted f^* is given in Eq. (1).

$$f^*(\phi) = [a\delta(\phi) + (1-a)f(\phi)] * e^{-\phi^2/2\sigma_b^2}. \qquad (1)$$

The paper is organized as follows. Sections II and III are a brief presentation of the GIFAD technique and elastic diffraction. Section IV reports the present status of inelastic diffraction and polar and azimuthal line profiles before analyzing experimental results. The overall line profile is characterized in Sec. V where its evolution with the projectile energy and angle of incidence as well as with the surface temperature and crystallographic direction is reported in dedicated sections. In particular, Sec. V B presents evidence that the overall azimuthal line shape does not depend on the probed crystal direction. Section V C compares the different forms of line profiles to data recorded in the quasiclassical region where elastic diffraction is weak and in the quasielastic region where it is dominant. It emphasizes that the proposed two-component profile representing the elastic and inelastic components allows a fair estimate of the Debye-Waller factor

TABLE I. Bragg angles ϕ_B under different conditions.

Direction	$d_\perp$	$G_\perp = 2\pi/d_\perp$	ϕ_B at 500 eV	ϕ_B at 5 keV
[100]	2.02 Å	3.11 Å^{-1}	0.183°	0.058°
[110]	2.85 Å	2.20 Å^{-1}	0.13°	0.04°

(DWF) from the azimuthal line shape close to the one derived from the decomposition of the polar profile. Similarities and differences between the overall polar and azimuthal profiles are also discussed. Section VI corresponds to restrictions of the above discussions to the azimuthal profile located on the Laue circle defined by $|\vec{k}_f| = |\vec{k}_i|$ where the elastic component is located so that the contrast with inelastic diffraction is maximal. The influence of the line profile on the determination of the diffracted intensities I_m is discussed here. Section VII extends to any value of the polar angle by investigating internal dependencies along θ_f and ϕ_f within a diffraction image. The quasielastic and quasiclassical regimes are characterized by different correlation schemes switching from a linear regime with the Laue circle as an absolute reference to a more complex polynomial behavior. Section VIII discusses the results from the perspective of simple models. Table III aggregates definitions of the geometry and angles used in this paper while Table IV reports definitions from previous simplified collision models.

II. GIFAD TECHNIQUE

The technique has been described in detail in Ref. [10] and only a brief presentation is sketched here. An ion beam of energy in the keV range is neutralized and drastically collimated to reduce its angular divergence below 0.01° before impacting on the target crystal surface at an incidence angle $\theta_i \sim 1°$. The particles reflected around the specular direction are collected onto a position-sensitive detector placed ~ 1 m downstream. By construction, this detector is perpendicular to the direction of the primary beam so that within minor corrections, the spatial coordinates (y, z) can be related to the final projectile velocity v_y, v_z (see Fig. 1). For convenience, we often use the associated wave vectors k_y, k_z. If the quality of the crystal surface is good enough, diffraction is present in the form of sharp spots on the Laue circle separated in the y direction by multiples of the reciprocal lattice vector $G_\perp \equiv G_y$, $k_{fy} = k_{iy} + mG_\perp$, where m is the diffraction order and the subscript i or f stands for the initial or final value. For well-aligned con-

TABLE II. Forms $f(x)$ used to describe the inelastic profiles. A is a normalization factor such that $\int_{-\infty}^{\infty} f(x)dx = 1$.

Name	Symbol	Formula	Variance
Expt. decay	E	$A \cdot e^{-|x/w|}$	$2w^2$
Gaussian	G	$A \cdot e^{-x^2/2\sigma^2}$	σ^2
Lorentzian	L	$A/(x^2 + w^2/4)$	undefined
$L(w) \cdot G(2w)$	$L \cdot G_2$	$A \cdot e^{-x^2/4w^2}/(x^2 + w^2/4)$	$\simeq 0.48w^2$
$L(w) \cdot G(w)$	$L \cdot G_1$	$A \cdot e^{-x^2/2w^2}/(x^2 + w^2/4)$	$\simeq 0.32w^2$
Log-normal	LN	$\frac{A}{xw} \exp(-\ln^2(\frac{x}{x_0})/2w^2)$	$\simeq w^2 x_0^2$

TABLE III. Definitions used in this paper.

k_{ix}, k_{iy}, k_{iz}	initial values of the projectile wave-vector $\vec{k}_i$
k_{fx}, k_{fy}, k_{fz}	final values, we assume $k_{fx} \simeq k_{ix}$
$k_\perp$	$\sqrt{k_y^2 + k_z^2}$, wave-vector in the perpendicular plane
$k_\parallel$	$k_{ix} \simeq k_{fx}$, wave-vector along x
θ_i	$\arctan(k_{iz}/k_{ix})$, incidence angle if $k_{iy} = 0$
θ_f	$\arctan(k_{f\perp}/k_{fx})$, polar scattering angle
ϕ_f	$\arctan(k_{fy}/k_{fx})$ lateral deflection angle Lab.frame
φ_f	$\arctan(k_{fy}/k_{fx})$ see Fig. 1
Laue circle	$k_{f\perp} = k_{i\perp} :=$ energy conservation in y, z plane see dotted white circle in Fig. 1
θ_s	$2\theta_i$, overall elastic scattering angle
$E_\perp$	$E_0 \sin^2 \theta_i$, perpendicular energy [8,9]
$d_\perp$	periodicity of the atomic rows $\perp$ to x

ditions ($k_{iy} = 0$), the Kapitza-Dirac obliquity factor [11,12] indicates that diffraction is present only along the y direction explaining that only one diffraction circle is observed (see also Refs. [13,14] for a quantum treatment or [15,16] for a classical approach). As a consequence, the relative intensities I_m can be measured at various combinations of the primary energy E_0 and θ_i giving the same value of $E_\perp = E_0 \sin^2 \theta_i$ [17]. A few degrees away from a low index direction, only the specular spot ($m = 0$) is present as with a perfectly flat mirror [18,19]. On LiF, only two crystallographic directions give rise to diffraction with $m \neq 0$, the [100] and the [110] directions. The periodicity $d_\perp \equiv d_y$, reciprocal lattice vector $G_\perp = 2\pi/d_\perp$, and associated Bragg angles ϕ_B are given in Table I. Taking the crystal normal as the z axis, the incidence and outgoing angles are listed in Table III.

TABLE IV. Definitions and formulas introduced in simplified collisions models [7,9,37,38] and mentioned in the discussion.

|		
———— (a)		Surface description
T_D, ω_D		Debye temperature and frequency $\hbar\omega_D = k_B T_D$
σ_z^2		variance of z position at a temperature T: $\langle z^2 \rangle_T$
$V_{1D}(z)$		mean planar potential: $\int_x \int_y \text{PEL}(x, y, z)$
———— (b)		binary collision model
m_p, m_t		projectile and target mass, $\mu = \frac{m_p}{m_t}$
E_r		$\mu E_0 \theta_b^2$, classical binary recoil energy where θ_b is the projectile deflection in this binary coll.
E_{loss}		ΣE_r, Classical energy loss
DWF		$e^{-E_{\text{loss}}/\hbar\omega_D}$ Debye-Waller factor for GIFAD
———— (c)		Purely repulsive collision model [7,9,37]
$V_r(z)$		$V_{1D}(z)$ is assumed to have the form $V_0 e^{-\Gamma z}$ with $\Gamma \sim 2\sqrt{2W}$ and W the work-function
Γ		Stiffness, logarithmic derivative $-\dot{V}_r(z)/V_r(z)$
E_{loss}		$\frac{2}{3}\mu E_0 \Gamma \theta_i^3$, Classical energy loss
N		$:= E_{\text{loss}}/E_r$, effective number of binary coll.
———— (d)		Collision model with attractive forces [38]
D		well depth of $V_{1D}(z)$
$E_\perp + D$		Beeby correction to the impact energy [56]
Morse pot.		$V_M(z) = De^{-\Gamma(z-z_0)} - 2De^{-\Gamma(z-z_0)/2}$
Γ_{eff}		defined as $-\dot{V}_M/V_M$ at the turning point z_t [38]
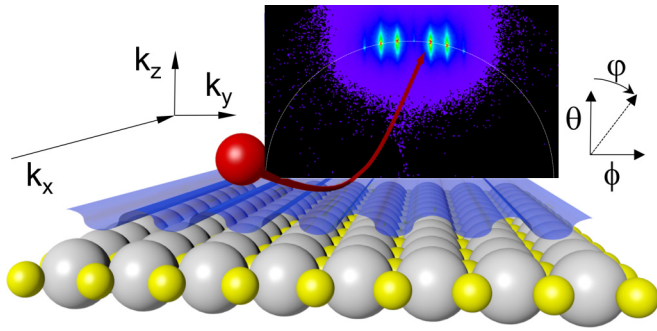
FIG. 1. Schematic view of a GIFAD experiment. The image is for 500 eV helium at $\theta_i = 1.56°$ along LiF[100] at $T = 167$ K.

III. ELASTIC DIFFRACTION

The elastic diffracted intensity derives from fully coherent scattering from perfectly periodic conditions. This corresponds to atoms at the equilibrium position, as if these were immobile. Using the Debye model, the surface atomic motion is described by a local oscillator, also called Debye oscillator or high-frequency limit, that after coupling between neighbors gives rise to the phonon modes as eigenstates of the system. The quantum aspect here is that the vibration is represented by a vibrational wave function and the probability that a surface atom exchanges the momentum δk, needed to deflect the fast projectile without changing its vibrational wave function, is the Lamb-Dicke probability [20]. In this case, the scattering by δk takes place from the center of the wave-function, i.e., from the equilibrium position. Consistently, quantum scattering calculations are usually performed directly from the equilibrium position [8,13,14,21–23] to represent elastic diffraction. Classical trajectories on this potential energy landscape (PEL) lead to a surprisingly well-defined Laue circle even with simplified binary collision models [20,24]. The diffraction spots are replaced by a continuous azimuthal profile showing a main rainbow and possibly secondary rainbows in the form of sharp singularities [25,26]. Attaching a semiclassical phase to the trajectories reveals the discrete structure of Bragg peaks and the modulation of the elastic diffracted intensity due to interference within the lattice unit. Supernumerary rainbows become visible when the phase difference below the rainbow angle exceeds multiples of 2π [17,18,27,28]. However, *ad hoc* additional treatments are needed to smooth the rainbow singularities [29] by an Airy-like profile or to account for the Gouy phase when passing through a focus [30]. For restricted shapes of the PEL, perturbation theory has also shown interesting results and delivered analytic expressions to describe atomic diffraction [31,32].

Diffraction of fast atoms has always been observed to be accompanied by an inelastic component, but the elastic intensity can be isolated and the slowly varying inelastic intensity suppressed by applying a simply doubly differential polar filter. This empirical approach produces an intensity located only on the Laue circle [5,33,34]. The associated azimuthal elastic profiles were found to be close to pure Gaussians having a width identical to the direct beam profile and justifying the use of the delta function $\delta(\phi)$ in Eq. (1).

IV. INELASTIC DIFFRACTION

Though most published results show a dominant inelastic intensity, the inelastic lateral profile has never been investigated extensively. Various empirical forms were proposed to fit the measured diffraction profiles. One is a combination of two Gaussians, a narrow one on top of a broader one with a relative weight a equal for all diffraction orders but evolving with incidence angle [9]. Another proposal was to use a Lorentzian [18,35] or a Voigt profile [36] irrespective of the elastic to inelastic ratio. In the present paper, new forms are introduced (as summarized in Table II) and the lateral profile is discussed in detail taking into account explicitly elastic and inelastic components. The two-dimensional (2D) color plot corresponds to the raw image in Fig. 1 after the polar transform of Ref. [5].

With a large band-gap insulator as LiF, probed with helium, the inelastic processes are expected to be governed by the interaction with surface phonons. At thermal energies and large incidences (TEAS) where the projectile hits a single surface atom, this gives rise to the well-known Debye-Waller factor describing the ratio of elastic intensity as proportional to $e^{-E_r/\hbar}$ where E_r is the recoil energy deriving from momentum conservation and ω_D is the Debye frequency (see Table IV). This is equivalent to the recoil-less Lamb-Dicke probability used to trap cold atoms.

In GIFAD, it was soon realized that the multiple collision regime specific to grazing incidences leads to a much more favorable DWF due to the fact that several (say N) tiny binary deflections by θ_b produce less decoherence than a single deflection by $2\theta_i = N \cdot \theta_b$. The DWF is now proportional to $\Pi_1^N e^{-E_r/\hbar\omega_D} = e^{-\Sigma_1^N E_r/\hbar\omega_D} = e^{-E_{loss}/\hbar\omega_D}$. It is the same formula but the recoil energy of a single binary collision is replaced by E_{loss}, the sum of all the classical recoils energies along the trajectories. It that can be calculated as $E_{loss} \simeq N \cdot E_r \propto E\theta_i^3$ assuming a purely repulsive form of the PEL [7,9,37] or a Morse form to account for attractive forces [see Table IV(c)].

The inelastic diffraction intensity is still partly coherent, as illustrated in Fig. 12 of Ref. [7], which shows that the intensities I_m can be extracted outside of the Laue circle, i.e., from purely inelastic intensity assuming an effective incident wave vector $k_{eff} = (k_{f\perp} - k_{i\perp})/2$ in the perpendicular plane. In other words, the relative intensities recorded on the circle of diameter k_{eff} encompassing the direct beam position (see. e.g., Ref. [5] for details) are close to the elastic one that could be recorded on the Laue circle if the angle of incidence would be $\theta_{eff} = \arctan(k_{eff}/k)$. The consequence is that on the Laue circle, both elastic and inelastic diffraction point to the same relative intensities I_m. This is compatible with the fact that all diffraction orders seem to have the same azimuthal line shape.

A. Inelastic polar profile

In terms of data analysis, the overall polar profile is defined in two steps. First, a simple polar transform of the 2D intensity $I(k_y, k_z) \rightarrow I(k_y, k_\perp)$, preserving the scattering plane and the direct beam position as invariant spot [5,7]. Second, a projection on $k_\perp$, i.e., an integration along k_y adding the polar profiles of all diffraction orders. Within a surprising accuracy, this polar profile visible in Fig. 2 was
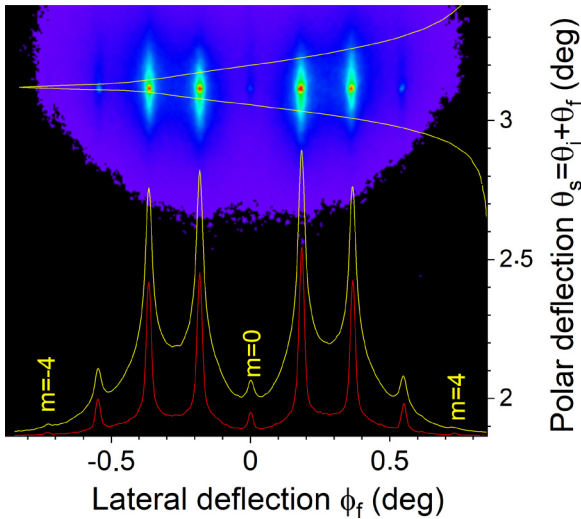
FIG. 2. The raw plot in Fig. 1 is polar transformed following Ref. [5]. The yellow lines are the overall polar and azimuthal profiles corresponding to intensity projections (full integration) while the red one is the intensity (x20) of a 0.015° band at the specular angle ($\theta_f = \theta_i$).

found to be independent of the probed crystal axis (see Fig. 4 of Ref. [38]). The polar profile is decomposed into a sharp central peak having a width similar to that of the primary beam sitting on top of a much broader one, well fitted by a log-normal shape (defined in Table II) as observed in fully inelastic conditions [39,40]. Interpreting these components as the elastic and the inelastic contribution, the $\log(DWF)$ was found to scale with $E\theta_i^3 T$ [41] as expected from Refs. [7,9,37]. The standard deviation σ_θ of this inelastic component was found to increase almost linearly with the angle of incidence θ_i so that the relative width $w \sim \sigma_\theta/2\theta_i$ (see Table II) is almost constant for 120 meV $\leqslant E_\perp \leqslant$ 500 meV while it increases rapidly below 120 meV [38,41]. These behaviors could be ascribed to classical scattering on thermally displaced surface atoms. The increase for $E_\perp \leqslant$ 120 meV could be related to the effect of attractive forces bringing the turning point of the trajectory closer to the surface and increasing the effective repulsion at this point. An effective surface stiffness Γ_{eff} [see Table IV(b)] was defined to describe this effect [38] first identified by Rieder *et al.* [42]. In GIFAD, the force at the turning point governs the momentum transfer to each surface atom and the inelastic effects. This will be discussed further with the results and in Sec. VIII.

V. OVERALL LATERAL LINE SHAPE

A. Overall lateral profile

The overall azimuthal scattering distributions either on the Laue circle or integrated over the polar angle are governed by the number of diffraction peaks rather than by their shapes [43]. It strongly depends on the probed crystal direction and the intensities I_m are a signature of the shape of the PEL [17,18,44] formed by the well-aligned rows of surface atoms. Monitoring the width of this overall azimuthal profile is enough to identify the crystal axis and corresponds to the

concept of atomic triangulation [17,43]. We focus here, not on the intensity I_m but on the line shape of these diffraction peaks. Since the first GIFAD observations, this later was reported to be identical for all diffraction orders of a given diffraction pattern [9,36].

B. Dependence on the crystal axis: ϕ scan

The independence of the lateral profile on the crystal axis was first suggested by Seifert *et al.* [36] who showed that the azimuthal profile recorded along a random direction could be used to fit the line shape of a low-index direction. No elastic diffraction was identified in this early work, but we found identical results with well-resolved elastic diffraction peaks. The finding could be due to the fact that when diffraction is observed the transverse coherence of the projectile is necessarily much larger than the unit cell so that only the mean number of collisions, directly connected with the target surface density is important. Independently of the exact mechanism, this seems to be true for the weakly corrugated LiF surface, as illustrated in Figs. 3 and 4 corresponding to perpendicular energies $E_\perp = 66$ meV and 365 meV, respectively. The overall profile recorded along a [Rnd] direction is compared with different line shapes in Figs. 3(a)–3(d) all convoluted by the direct beam profile (Table II). The Lorentzian L^* form in Fig. 3(a) has a too-large tail while the Gaussian one G^* in Fig. 3(b) has a too-short tail. In Figs. 3(c), 3(d) the data are equally well fitted by an exponential decay form E^* or by the bounded Lorentzian ($L.G^*$ in Table II) where the Lorentzian function of width w is multiplied by a Gaussian function forcing the extinction of the long Lorentzian tail. $L \cdot G_1^*$ is for a Gaussian with $\sigma = w$ while $L \cdot G_2^*$ is for
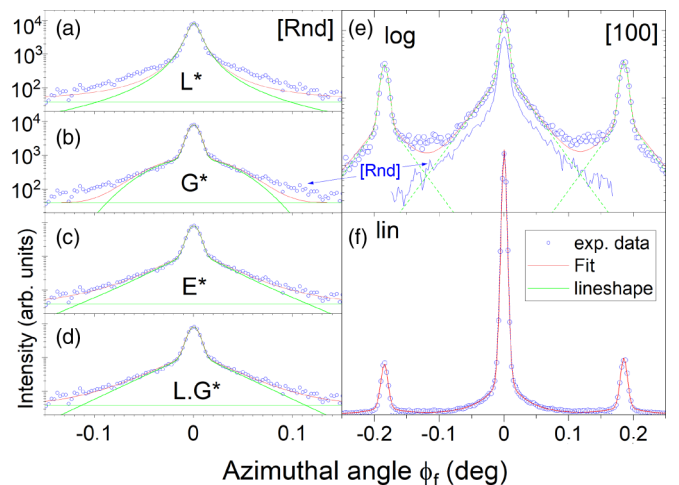

FIG. 3. The scattering patterns of 500 eV He atoms impinging at $\theta_i = 0.66°$ ($E_\perp = 66$ meV, $E\theta^3 = 0.76$ meV) on LiF at $T = 180$ K. The left panels (a)–(d) are for a random direction [Rnd] compared with a Lorentzian, Gaussian, exponential, and bounded Lorentzian, respectively. The right ones are for a [100] direction in linear (f) and log scale (e). The blue line in (e) is the raw profile in (a)–(d) while the green lines in (e) and (d) are the convolution of a pure exponential decay with a range $\phi_0 = 0.031°$ by the beam profile with $\sigma_b = 0.006°$. $f(\phi)^* = (0.52\,\delta(\phi) + 0.48\,A e^{-|\phi/\phi_0|}) * e^{-\phi^2/2\sigma_b^2}$.
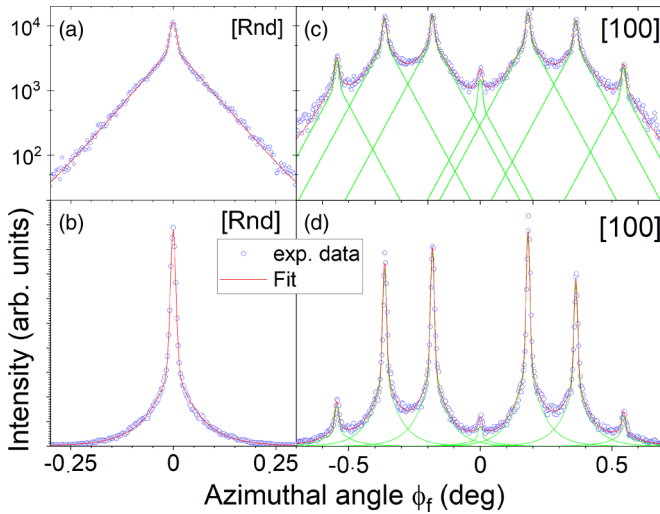
FIG. 4. The scattering pattern of 500 eV He atoms impinging at $\theta_i = 1.54°$ ($E_\perp = 365$ meV) on LiF at $T = 180$ K. Left panels (a), (b) are for a random direction while the right ones (c), (d) are for a [100] direction. Top panels (a), (c) are in log scale. Both directions are well fitted with a unique line shape, the a value indicates an inelastic ratio of 83% while the exponential decay range ϕ_0 is here 0.06°.

$\sigma = 2w$ and both produce a decent fit with comparable values of σ_ϕ.

Figures 3(e), 3(f) display in log scale and linear scale, respectively, the overall azimuthal profile recorded at the same energy and incidence angle but along the [100] direction. The blue line reproduces the profile Figs. 3(a)–3(d) recorded along the [Rnd] direction, while the green lines are the line shape used to fit the data. This line shape is identical to the one used to fit the [Rnd] direction in Fig. 3(c).

A similar comparison is repeated for an incidence angle of 1.54° and displayed in Fig. 4. The perpendicular energy $E_\perp$ is now 365 meV and inelastic diffraction dominates. Here again, the scattering profile recorded along a [Rnd] direction is well fitted by either an E^* or $L \cdot G^*$ profile. Using the exponential decay form, the decay range is now $\phi_0 = 0.06°$ (compared to $\phi_0 = 0.03°$ at a lower energy in Fig. 3) and the weight of inelastic diffraction is 83%, almost twice as large as in Fig. 3. Figures 4(c), 4(d) show the overall azimuthal profiles recorded along the [100] direction for identical beam parameters together with the fit by the profile derived from the [Rnd] direction. The quality of the fit, both in linear and log scale suggests that indeed, the line profile does not depend significantly on the probed crystal axis. From Figs. 3 and 4, it is clear that the shape of the far wings of the lateral profile can only be investigated along a [Rnd] direction.

C. Choice of functional form

Figures 3 and 4 show that for perpendicular energies of up to 400 meV, both the pure exponential decay and the bounded Lorentzian profiles give a very good description after convolution by the beam profile. For larger values of $E_\perp$, as shown in Fig. 5 recorded at $\theta_i = 2.36°$, i.e., $E_\perp = 850$ meV, a clear departure from the simple exponential decay can be observed.
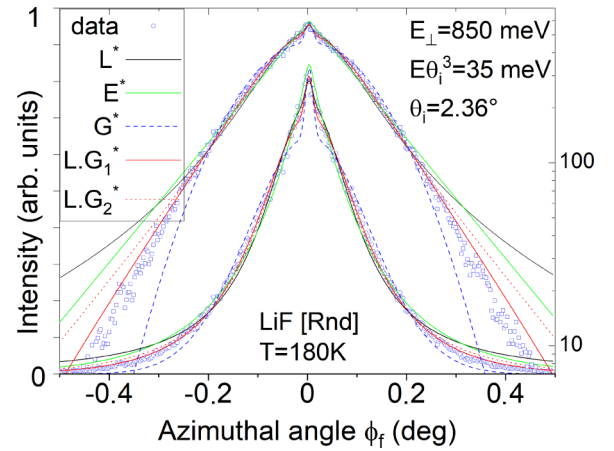

FIG. 5. Overall line profile of 500 eV He atoms impinging at $\theta_i = 2.35°$ on LiF at $T = 180$ K. The same data are plotted in linear (○ on left) and log scale (□ on right). The $L.G_1^*$ form provides the best fit. Depending on the line shape, the elastic intensity [a in Eq. (1)] varies by a factor ~ 3.

The $L \cdot G_2^*$ gives the best fit but slightly overestimates the length of the tail. The $L \cdot G_1^*$ form in Table II produces a faster attenuation of the tail. At even larger values of $E_\perp$, around 2 eV, the lateral profile is best fitted by a simple Gaussian form (not shown).

D. Dependence on the primary energy: *E* scan

Figure 6 reports the azimuthal linewidth measured during an E scan performed along a [Rnd] direction and with a fixed incidence angle of 0.66° with primary energy varied between 300 eV and 3 keV. For all energies, the overall scattering profiles of the single diffraction peak is well fitted either by E^* or by the two $L \cdot G^*$ forms. The ratio of elastic diffraction (a in Table II or DWF) drops by two orders of magnitude, from around 60% at 300 eV ($E_\perp \sim 40$ meV) below a fraction
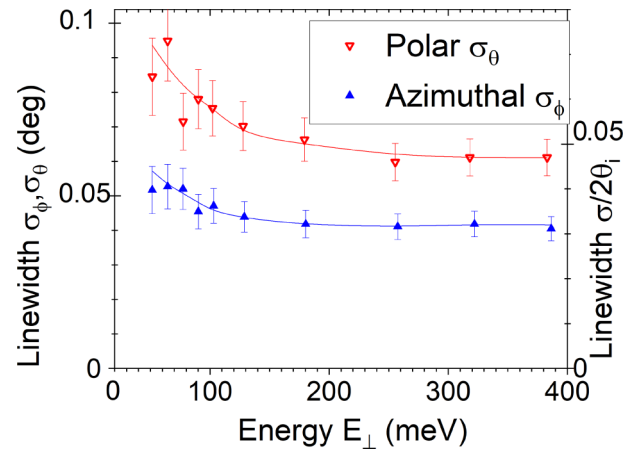

FIG. 6. The polar (σ_θ ▽) and azimuthal (σ_ϕ ▲) widths of the overall inelastic profile recorded along a [Rnd] direction during an E scan at a fixed incidence angle $\theta_i = 0.66°$ are reported as a function of the perpendicular energy $E_\perp$ with lines to guide the eyes. The scale on the right-hand side shows the dimensionless unit $\sigma/2\theta_i$ used in Refs. [7,38,41].
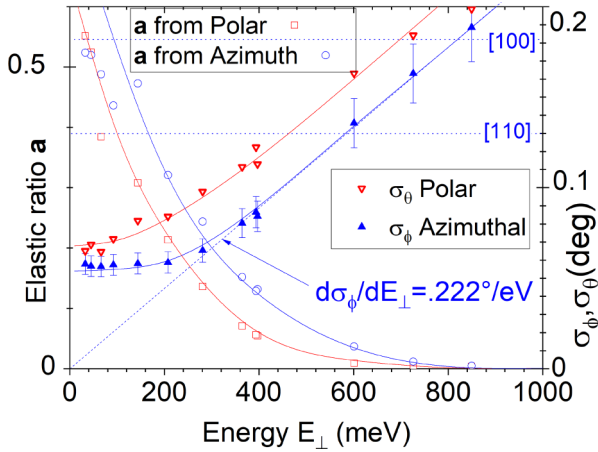
FIG. 7. Evolution of the azimuthal σ_ϕ (▲) and polar σ_θ (▽) widths during a θ scan at $E = 500$ eV along a [Rnd] direction where only the specular peak is present. The coefficient a in Eq. (1) represents the elastic ratio extracted from a fit of the azimuthal (○) or of the polar profile (□). The lines are to guide the eyes.
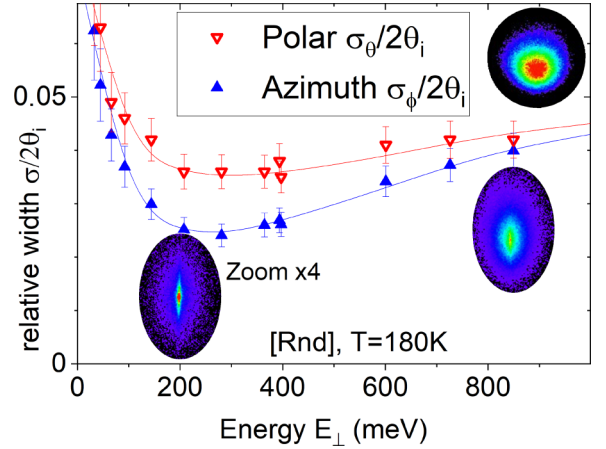

FIG. 8. The same polar and azimuthal widths as in Fig. 7 are plotted as a dimensionless relative widths $\sigma_\phi/2\theta_i$ (▲) and $\sigma_\theta/2\theta_i$ (▽) used in Refs. [7,38]. The lines are to guide the eyes. Inserts are 2D(ϕ, θ) profiles at $E_\perp = 200$ and 850 meV, the one in the top right corner was recorded separately at 3 keV and 3.5° ($E_\perp \simeq 10$ eV) and is compressed nine times.

of a percent at 3 keV ($E_\perp \sim 400$ meV), but the width σ_ϕ of the inelastic contribution appears almost constant over the whole energy range. This is also the case for the polar width σ_θ over the same energy range. The surprise is that σ_ϕ and σ_θ have a comparable magnitude. This contradicts the visual aspect of a very elongated spot as visible in the inset at 850 meV in Fig. 8 corresponding to the maximum energy where the elastic contribution is still clearly visible but very weak. The reason is that the associated line shapes are very different, log-normal polar profile [38] has a flat top but short wings, whereas the azimuthal one, has a sharper peak but a broader base giving different visual aspects but comparable variances or standard deviations.

As a simplifying summary, during an E scan, the inelastic component has almost constant polar and azimuthal width so that the overall line shape is simply a variable combination of this fixed inelastic shape plus the narrow elastic one. We now try to investigate the evolution of the line shape with the angle of incidence.

E. Dependence on the angle of incidence: θ scan

Using the same procedure and functional forms, Fig. 7 reports the evolution of σ_ϕ and σ_θ *vs* $E_\perp$ corresponding to a comparatively large angular range, between 0.3° and 2.5° for 500 eV helium on a LiF surface at 180 K oriented along a [Rnd] direction. Here again, σ_ϕ and σ_θ have a comparable magnitude and now increase rapidly with $E_\perp$ above 200 meV. The elastic ratio derived from the fit of the polar and azimuthal profiles do not coincide perfectly but show comparable trends compatible with previous investigations using only the analysis of the polar profile [41]. The horizontal lines at $\phi = 0.13$ and 0.186° in Fig. 7 correspond to the value of the Bragg azimuthal angle ϕ_B associated with the [100] and [110] directions. Typically, inelastic diffraction features should become difficult to observe when the inelastic width σ_ϕ exceeds the peak separation ϕ_B. Note that the width of the elastic diffraction remains narrow, but its relative intensity given by the

Debye-Waller factor becomes very weak. To summarize the θ scan, above $E_\perp \sim 200$ meV, the inelastic azimuthal width σ_ϕ scales linearly with $E_\perp$ at a rate given by $d\sigma_\phi/dE_\perp = 0.222°$/eV. To explore beyond this linear dependence, Fig. 8 reports the width σ_θ and σ_ϕ relative to the angle of incidence θ_i (or to the specular scattering angle $\theta_s = 2\theta_i$) canceling the linear increase in Fig. 7. The evolution now compares with the one observed in Fig. 6 during an E-scan. As a difference, the comparatively flat section above $E_\perp = 200$ meV is replaced by a smooth increase of both σ_θ and σ_ϕ with a possible convergence around $E_\perp = 1$ eV.

The log-normal shape was introduced empirically for its good description of the asymmetric polar profile [40]. It was later derived as the natural scattering distribution emerging from a binary collision with a Gaussian thermally distributed surface atom [7,37]. The constant ratio of $w \simeq \sigma_\phi/2\theta_i$ is therefore linked to a simple scattering property. The azimuthal relative width $\sigma_\phi/2\theta_i$ introduced here can be interpreted as the azimuthal width σ_φ expressed in the polar coordinates (φ, θ) instead of (ϕ, θ) as depicted in Fig. 1.

The 2D(θ, ϕ) scattering profiles at $E_\perp = 200$ meV and 850 meV are reported in Fig. 8 and show the evolution towards a more circular pattern with increasing perpendicular energy. Here again, the difference in line shape along θ and ϕ explains that, even when σ_ϕ is close to σ_θ, the impression of an elongated spot prevails. Exploring much larger energies and angles we could find situations where σ_ϕ becomes larger than σ_θ (top right insert in Fig. 8).

Focusing on the DWF, the evaluations from the polar profile using Eq. (1) with a $LN(\theta)$ or from the lateral profile with $L \cdot G(\phi)$ are completely independent and should give identical values. The results indicated by (□) and (○) symbols in Fig. 7 show similar tendencies but also significant differences at low values of DWF probably due to shape-specific difficulties to isolate an elastic contribution below a few % from the polar or azimuthal profile. It should also be noted that taking the exact value σ_b measured on the direct beam to fit the elastic lateral

profile always gives a good result, whereas, for very grazing incidence, Ref. [38] indicates a tendency that a good fit of the polar profile requires a weak broadening of σ_b.

F. Summary on the overall azimuthal width

The overall azimuthal scattering profiles have been analyzed in terms of the line shape of the diffraction peaks. For the conditions investigated here, the line profile does not depend on the diffraction order so a unique line shape can be used to fit the overall azimuthal profile. This inelastic line shape has a comparatively sharp peak and long tails. At low incidence angles where the elastic contribution dominates, it is almost impossible to assess the exact shape of the peak, a simple exponential decay provides a good fit. We found that the inelastic azimuthal line shape is well reproduced by a Lorentzian profile multiplied (attenuated) by a Gaussian function and convoluted by the beam resolution $L \cdot G^*$ [7] (Table II). During an E scan, the line width σ_ϕ appears rather stable while during a θ-scan, it also appears stable for values of $E_\perp < 200$ meV but increases rapidly above. When divided by the specular scattering angle $\theta_s = 2\theta_i$, the polar and azimuthal widths have a comparable behavior illustrated in Fig. 8. The next sections will investigate the same properties but restricted to the Laue circle, i.e., without integrating over the polar direction.

VI. LINE SHAPE ON THE LAUE CIRCLE

We now focus on the intensity sitting on the Laue circle where the elastic intensity is maximum. Considering a narrow polar band of approximately the beam width σ_b on the Laue circle (in practice a narrow crescent disk [5]), the weight of the elastic peak is on the order of σ_θ/σ_b larger than on the overall azimuthal profile investigated in the previous section. We first recall that, when elastic diffraction is observed, the elastic and inelastic relative intensity I_m on the Laue circle were found to be equal [7]. Therefore, it is not needed to separate elastic and inelastic contributions precisely. We use the same procedure and functional forms but the coefficient a in Table II describing the relative weight of the elastic peak is now interpreted as the visibility of elastic diffraction, not as the DWF. In general, the inelastic width σ_ϕ measured on the Laue circle is smaller than when measured on the overall profile but it differs only by 10–20 %. Taking the example of the overall azimuthal profile displayed in Figs. 4(c), 4(d) where a 17% DWF was estimated, the same fit restricted to the Laue circle gives a visibility of 49% instead, while the inelastic azimuthal width σ_ϕ is reduced by 10%. Hence, the dominant effect on the peak profile is the drastic increase in the ratio of the elastic component.

We explore below two situations where neighboring diffraction peaks overlap due to a small Bragg angle and/or to a significant inelastic broadening. Measuring a small diffracted intensity in the vicinity of intense peaks becomes difficult and sensitive to the line shape. For simple crystals where only one maximum and one minimum of the electronic density are present in the lattice unit, only two semiclassical trajectories interfere at a given scattering angle ϕ_f as illustrated in Figs. 2–4 of Ref. [18]. A simple ray-tracing model
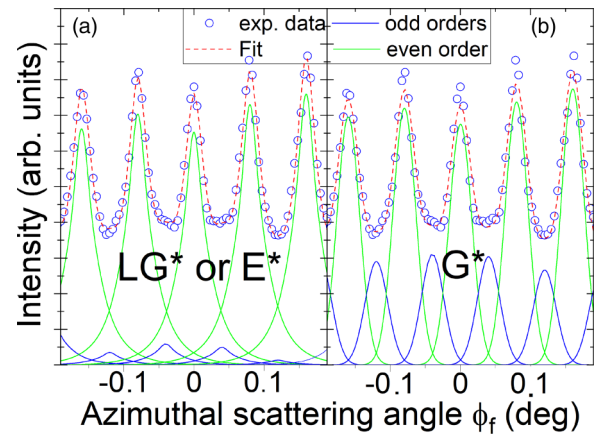

FIG. 9. The central part of the diffracted intensities along LiF [110] at 5 keV and $0.75°$ ($E_\perp = 865$ meV) is fitted by two line profiles of Table II. (a) $L.G^*$ (E^* gives equivalent results) (b) G^*. The odd diffraction orders in blue are expected to be weak (see text) and this is better reproduced by the fit in (a). The elastic weight is estimated at around 5% from the polar profile and is hardly visible here.

indicates that for small lateral deflection, i.e., the rays emitted from the top of F^- or Li^+ ions and separated along y by $d_\perp/2$ are π shifted so that the intensity of the odd orders oscillates in opposition to that of the even diffraction orders [33]. On LiF and for values of $E_\perp < 1$ eV, this is true both along the [100] and [110] directions (see, e.g., the diffraction charts in Fig. 3.21 of Ref. [18] or Fig. 2 of Ref. [44] where each bright diffraction order is surrounded by dark one in the central region). It means that for these directions, whenever a central peak reaches its maximum intensity, the adjacent peaks should be weak and vice versa.

Figure 9 displays the central part of the azimuthal profile recorded with 5 keV helium along the [110] direction at $0.75°$ incidence where all even diffraction orders ($m = 0, \pm 2, \pm 4$) are quite intense. We have tried to evaluate the influence of the line shapes on the extracted intensities with the idea that the odd diffraction orders should have an intensity as low as possible without turning negative. This is only qualitative but the mean level of the odd diffraction orders is low with the $L \cdot G^*$ and the exponential decay profile E^* whereas it is quite large with the Gaussian G^* line shape and produces some negative values with the Lorentzian profile L^* (not shown). Another indication that the Lorentzian profile produces too broad wings was identified close to the rainbow scattering angle corresponding to a maximum of the classical deflection function [17,27]. At this angle, several classical trajectories are scattered at the same angle and quantum mechanically the associated diffraction orders tend to have comparable phases and a significant intensity. The use of a Lorentzian profile was found to produce an exaggerated intensity level extending to scattering angles beyond the rainbow angle [7].

A more quantitative strategy to evaluate the quality of the line shape is to compare intensities I_m recorded at very different E_0 and θ_i conditions but with identical values of $E_\perp = E_0 \sin^2 \theta_i$ so that I_m should be identical [13]. Figure 10 reports diffracted intensities recorded at 300 eV and 5000 eV and incidence angles of $1.35°$ and $0.33°$, respectively so that
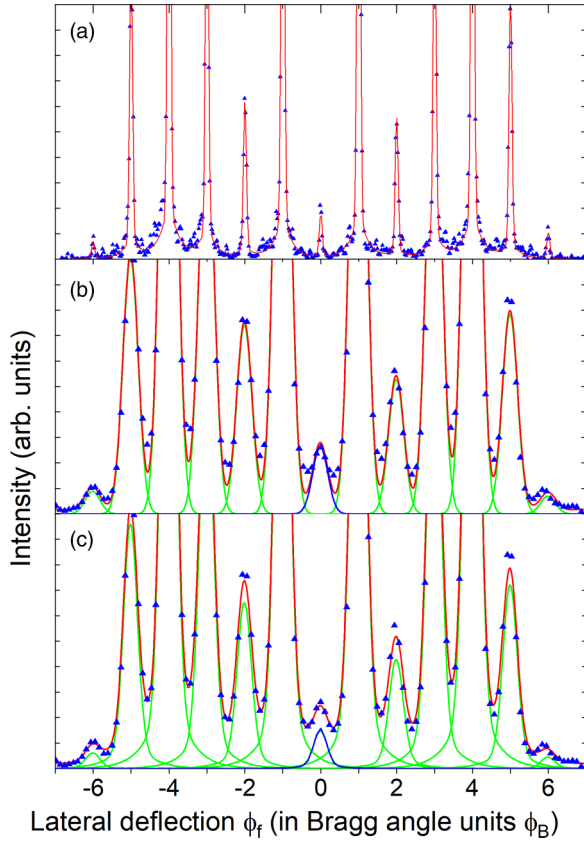
FIG. 10. Diffracted intensities recorded with He on LiF [110] at (a) 300 eV, $\theta_i = 1.35°$ and (b), (c) 5000 eV and $\theta_i = 0.33°$. Both correspond to $E_\perp \sim 165$ meV and were recorded with an angular resolution $0.007°$ ($0.016°$ FWHM). The red lines correspond to a fit through the data using a common line shape for all peaks. (b) is fitted by a pure Gaussian while (a) and (c) correspond to the profile $E^*(\phi)$ in Table II. The contribution of the specular peak (blue line) depends on the line shape.

the energy $E_\perp$ is close to 165 meV in both cases. The angular resolutions are both around $0.007°$, but they appear quite different on the detector as the radius of their Laue circle varies by a factor ~ 4. In Fig. 10(a), the diffraction peaks are well separated and even a poor description of the profile will not alter the derived I_m. Oppositely, Figs. 10(b) and 10(c) correspond to the smaller Laue circle recorded at 5 keV where the diffraction peaks overlap enough to influence their maximum intensity. The quality of the fit by a Gaussian G^* in Fig. 10(b) is less than by E^* or $L \cdot G^*$ in 10(c) but the main result is that only the intensities I_m derived from the E^* or $L \cdot G^*$ functional forms compare quantitatively with the values derived at 300 eV in Fig. 10(a). For instance, the intensity I_0 of the specular peak ($m = 0$ in blue) is overestimated by almost 50% in Fig. 10(b) whereas the value measured in Fig. 10(c) differs by only 10% from the value determined in Fig. 10(a) where the peaks are well separated.

VII. CORRELATIONS BETWEEN θ_f AND ϕ_f

By investigating either the overall distribution or the one on the Laue circle, we have bypassed the internal correlation of
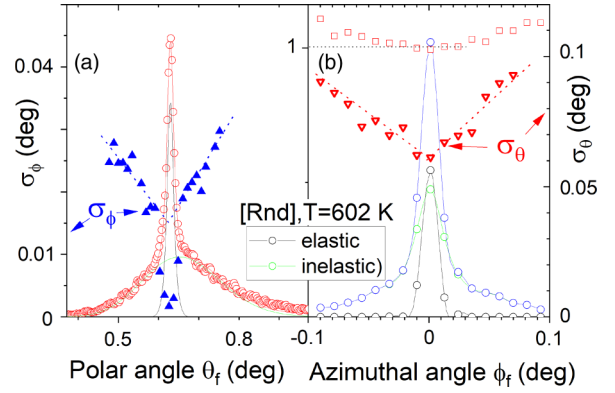

FIG. 11. For 500 eV helium scattered along a [Rnd] direction at $\theta_i = 0.628°$ incidence ($E_\perp = 60$ meV and $E\theta^3 = 0.66$ meV), the (a) polar $\circ$ and (b) azimuthal $\circ$ profiles are decomposed into elastic $\circ$ and inelastic $\circ$ components. The standard deviation of the azimuthal $\blacktriangle$ and polar $\triangledown$ distributions show a linear increase away from elastic conditions, dotted lines are to guide the eyes. The $\square$ symbol represents $\overline{\theta}_f/\theta_i$ and shows the weak variation of the mean polar scattering angle.

the 2D intensity distribution. We analyze here this correlation for diffraction along a random direction. For each value of θ_f, the distribution of ϕ_f has properties that are different on the Laue circle ($\theta_f = \theta_i$) and far away from the Laue circle. We observe no dependence of the mean azimuthal scattering angle $\overline{\phi}_f$ with the final polar angle θ_f and a weak evolution of the mean polar angle $\overline{\theta}_f$ with the final azimuthal angle ϕ_f. This is not the case for the width σ_ϕ. In Sec. VI, we indicated that within typically 10%, the widths σ_ϕ measured on the Laue circle compare with the ones measured on the overall azimuthal profile. This is mainly due to the fact that the intensity on the Laue circle is maximum and its contribution dominates the average. We try below to analyze in more detail the specificity of the Laue circle.

A. Lateral width σ_ϕ versus θ_f

At small values of $E\theta_i^3T/300$ where elastic diffraction dominates, the evolution of the inelastic line shape above or below the Laue circle is quasisymmetric, the line width increases almost linearly with the distance to the Laue circle; $\sigma_\phi = \sigma_{\phi_s} + \alpha|d\theta|$ where σ_{ϕ_s} is the value measured on the Laue circle (at specular angle θ_{spec}) and $d\theta = \theta_f - \theta_i$ is the distance to the Laue circle. This indicates that the specular condition is indeed a reference for the inelastic process. Any departure from this reference either upward or downward is accompanied by a significant increase in the width. This is illustrated in Fig. 11(a) where the blue triangles represent the standard deviation of the azimuthal distribution as a function of the polar angle θ_f. The width is measured by simple statistical evaluation of the variance $\sigma_\phi^2 = \Sigma_\phi I(\phi)\phi^2/I_{\text{tot}}$ without trying to separate the elastic and inelastic contributions. As a consequence, the sharp dip around the specular polar angle simply outlines that, at this location, the azimuthal distribution is dominated by the narrow elastic spot. This dip, outlining the elastic contribution, could be bypassed by fitting the profiles to isolate the inelastic contribution but the fit is partly
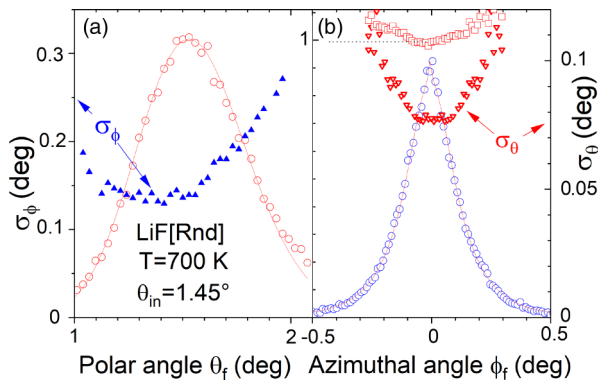
FIG. 12. For 500 eV helium scattered along a [Rnd] direction at $\theta_i = 1.45°$ incidence ($E_\perp = 320$ meV and $E\theta^3 = 8.1$ meV), the (a) polar ○ and (b) azimuthal ○ profiles are reported showing no clear elastic component. The standard deviation of the azimuthal ▲ and polar ▽ distributions show a diffuse minimum and a possible quadratic dependence. The □ symbols represent $\overline{\theta}_f/\theta_i$ and show the weak variation of the mean polar scattering angle.

unstable, probably because the elastic component is so large that a variation as small as 0.1 pixel of its line shape [σ_b in Eq. (1)] significantly affects the fit. For Fig. 11(a), the width σ_{ϕ_s} at the specular angle is estimated by interpolation as $\sigma_{\phi_s} \simeq 0.015°$ and the slope α is close to 0.1 meaning that the σ_ϕ increases by $0.01°$ every $0.1°$ away from the Laue circle.

At larger values of $E\theta_i^3 T/300$ where the elastic component is much weaker than the inelastic one, the evolution of the line width becomes asymmetric. The position of the minimum line widths shifts to underspecular conditions ($\theta_f < \theta_i$) as illustrated in Fig. 12(a) recorded with a surface at 700 K. Figure 13 recorded at room temperature but with 4 keV projectiles explores fully inelastic condition with $E\theta^3$ above 40 meV where the DWF is probably less than 10^{-8} [41]. The shift $\delta\theta$ between the maximum intensity and the minimum of the line width is
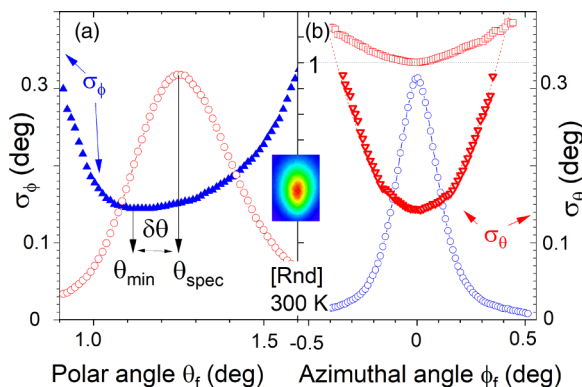

FIG. 13. Same as Figs. 11 and 12 with 4 keV He projectiles at 1.25° ($E\theta^2 = 1.9$ eV, $E\theta^3 = 41$ meV). No elastic component is visible in the (a) polar ○ and (b) azimuthal ○ profiles. The standard deviation σ_ϕ▲ of the azimuthal distribution associated with a polar angle θ_f shows a minimum located at θ_{min} well below the specular scattering angle θ_{spec}. The polar width σ_θ▽ has a quadratic behavior ($\sigma_\phi \sim 0.14 + 1.4\phi_f^2$). The mean scattering angle $\overline{\theta}_f/\theta_i$(□) varies weakly with ϕ as in Figs. 11–12.

more pronounced than that of Fig. 12 in spite of a smaller angle of incidence.

B. Polar width σ_θ versus ϕ_f

This section is in part beyond the main focus of the paper but is reported here for completeness. We investigate the evolution of the polar width σ_θ as a function of the departure from the Bragg condition $\phi_f = mG_y$. Under a random direction where only $m = 0$ is present, the reference is the scattering plane $\phi_f = \phi_{m=0} = 0$.

The mean value of the polar distribution $\overline{\theta}_f/\theta_i$ depends only slightly on the azimuthal angle ϕ_f as indicated by red hollow square symbols (□) in Figs. 11(b), 12(b), and 13(b). For values of ϕ_f within the FWHM of the azimuthal profile, the variation of $\overline{\theta}_f/\theta_i$ is less than 5%.

The variation of the polar width σ_θ with ϕ_f (▽) is more pronounced and is comparable to that of the azimuthal width σ_θ with θ_f (▲). At low values of $E\theta^3$ in Fig. 11(b) the dependence is linear while it shows a flat minimum close to $E\theta^3 \simeq 10$ meV, the observation threshold of elastic diffraction in Fig. 12(b). In Fig. 11(b), a fit was needed to isolate the inelastic contribution while a straightforward statistical evaluation was performed in Fig. 12(b). At much larger values of $E\theta^3$, a regime where elastic diffraction cannot be observed, Fig. 13(b) indicates a pronounced quadratic behavior.

VIII. DISCUSSION

For large band-gap insulators like LiF, the inelastic effect in diffraction is dominated by interaction with phonons [37]. With atoms at thermal energies and quasinormal incidence, energy-resolved inelastic diffraction reveals the specific surface phonon modes [45] and, for metals, the coupling could be traced to the strength of the electron-phonon interaction [46–48]. In GIFAD, the total energy cannot be resolved in the meV range and, so far, only the scattering in the perpendicular plane can be analyzed.

The theory also is much less developed due to the more complex regime where the projectile interacts with many surface atoms. An attempt to account for the actual phonons modes involved in the scattering within a quantum treatment [49,50] seems to indicate a dominant contribution of long wavelength acoustic modes but no scattering distribution was produced to be compared with experiments. Random kicks to the projectile wave packet were proposed [21,51] to simulate inelastic profiles with properties resembling experimental data but elastic diffraction is absent and quantitative agreement was not demonstrated. Using a semiclassical approach, other authors proposed [52–54] to expand the surface thermal motion in terms of the number n of exchanged phonons labeled Pn-SIVR (for surface initial value representation). However, from our point of view, the P0-SIVR, assumed elastic, produces a distribution having all the properties of inelastic diffraction: It has a log-normal profile with a relative polar width $w = \sigma_\theta/2\theta_i$ only slightly lower than the measured ones [52]. It stays remarkably constant during an E scan [54] for $E_\perp$ above 200 meV as in Fig. 6 and it follows the observed evolution with the surface temperature [41]. Here also, there is no sign of a narrow elastic peak and, if the P0-SIVR is interpreted

as inelastic, then all the other terms of the expansion should be present. More problematic, in terms of application, the approach predicts a very strong variation of the diffracted intensities I_m on the Laue circle with the temperature [53,54], which is not observed in GIFAD [41] neither in TEAS [55], apart from lattice thermal expansion. This can probably be traced back to the fact that neither the random kick nor the SIVR approaches do consider the Mösbauer-Lamb-Dicke effect [7], which is a quantum effect (without classical equivalence but uses thermally displaced atoms so that the mean potential probed by the trajectories is different from the one at equilibrium [7,51] and becomes temperature dependent.

Simplified models have been developed to connect the polar and azimuthal profiles to thermal surface properties. The interaction with the complex phonon system is replaced by successive independent quantum binary collisions with the local (Debye) harmonic oscillator representing the surface atom, taking place along the elastic trajectory [7,37]. Each is contributing (if inelastic) to the final inelastic angular widths σ_ϕ and σ_θ by an elementary (binary) broadening calculated in the classical eikonal approximation. For a purely repulsive exponential PEL, the scattering profile of a single binary collision is a log-normal profile with a relative width $w_b = \Gamma \sigma_z \simeq \sigma_{\theta_b}/\theta_b$ where σ_z is the amplitude of the thermal motion of a surface atom along z [7]. The DWF is derived from the assumption that one such inelastic collision is enough to drive the trajectory inelastic. This seems to fit the experiment [41] but the expansion of the polar inelastic profile in terms of the number of inelastic collisions proposed in Ref. [7] does not. Instead, the inelastic polar profile was found to have always the maximum width $\sigma_\theta^2 = N\sigma_{\theta_b}^2$. As if a single inelastic collision (among N) is enough to induce a quasiclassical scattering profile where all N binary collisions become inelastic and contribute to the broadening [38]. In this respect this is equivalent to the near-classical scattering with spatial correlations of Ref. [37].

When investigating the effect of attractive forces, two additional effects were found important [38]: The Beeby correction factor [56] considers that the impact energy $E_\perp$ should be replaced by $E_\perp + D$ where D is the depth of the attractive well [see Table IV(d)]. As in TEAS [57], this correction is significant for elastic diffraction only at low energy, when $E_\perp \sim D$ [58], which is here less than 10 meV [59]. It also influences the DWF in TEAS but hardly does so in GIFAD due to the multiple collision regime [38]. The effective stiffness Γ_{eff} describing the modification of the repulsive forces due to the attractive terms at the turning point z_t has no major consequence in TEAS [42] whereas in GIFAD it was found responsible for the rapid increase of σ_θ/θ_i at values of $E_\perp$ below 200 meV [38,44] as visible here in Figs. 6 and 8. In these figures, σ_ϕ and σ_θ have a comparable behavior suggesting that attractive forces are also responsible for the increase of σ_ϕ/θ_i below $E_\perp = 200$ meV. Both Γ_{eff} and z_t are detailed in Ref. [38].

Focusing on the differences between azimuthal and polar line widths, we return to the perturbative approach [7] where these scattering profiles result from the self-convolution of the binary collision profile. The log-normal inelastic polar profile was first derived assuming only a surface atomic motion along z and a projectile trajectory exactly on top of an atomic row

where the force is only vertical so that no lateral deflection is possible ($\sigma_\phi = 0$).

Considering in-plane motion along y produces a narrow azimuthal Gaussian profile with σ_ϕ of only a few mdeg. It was then proposed to average the scattering properties over all possible impact parameters y within the transverse coherence [7,20] (in practice over the lattice unit $d_\perp$). On one hand, the azimuthal profile became significantly broader and was modeled as having a general $L \cdot G$ shape [7], i.e., a comparatively sharp Lorentzian peak but with attenuated wings (Table II). On the other hand, the polar profile keeps its log-normal character but with a width reduced by 30% because the momentum transfer is not exactly vertical anymore. This redistribution between lateral and vertical deflection, quantified by the ratio of σ_ϕ to σ_θ, depends in part on the elevation z_t of the turning point and should therefore increase from low to high values of $E_\perp$. On the low-energy side, the ratio should be stable because the attractive force brings the turning point z_t close to z_c, the edge of the attractive well (which is reached even for $E_\perp = 0$). On the high-energy side, Fig. 8 indicates that σ_ϕ gets closer to σ_θ and the top right inset, taken at $E_\perp \simeq 10$ eV shows that σ_ϕ becomes larger than σ_θ. This happens for deeply inelastic conditions where the trajectories could become localized and where the validity of the above model constructed around elastic trajectories with surface atoms at equilibrium is probably limited. These very qualitative features remain to be confirmed by numerical simulations and quantitative comparisons but they suggest a possible difference to the diffraction of x rays, neutrons, electrons, and positrons where the in-plane motion of surface atoms is considered as the dominant contribution to lateral broadening of the inelastic peaks. The physical origin suggested here would be that the scattering of atoms does not take place close to the nuclei of the surface atoms.

IX. SUMMARY AND CONCLUSION

We have investigated the lateral line shape both associated with the overall scattering profile or restricted to the Laue circle. The first important conclusion is a clear confirmation of the previous findings by Seifert *et al.* [36] that the azimuthal diffraction line shape does not depend on the crystallographic axis. We have clarified the issue by separating the elastic and inelastic contribution and by using, for the inelastic component, analytic forms convoluted by the primary beam profile [see Eq. (1)]. A broad range of physical conditions within the quantum and semiclassical regime where elastic diffraction can be observed has been investigated. With the present helium-LiF system, this regime corresponds to values of $E\theta^3 \leqslant 10$ meV. For very low values of $E\theta^3 \leqslant 3$ meV, the inelastic line shape is equally well described by either a pure exponential decay (E^* in Table II) or by the product of a Lorentzian by a Gaussian ($L \cdot G_1^*$ or $L \cdot G_2^*$ in Table II). At values of $E\theta^3$ exceeding several tens of meV only inelastic diffraction is present and the azimuthal width increases progressively beyond the Bragg angle ϕ_B leaving only a smooth modulations of the azimuthal intensity [17,27] and progressively vanishing. At even larger values, the line shape evolves to a Gaussian profile with a width σ_ϕ much larger than ϕ_B and the last quantum effect is the principal rainbow azimuthal

profile, which eventually becomes weaker than the azimuthal width. Following the analysis of the polar profile with temperature between 177 K and 1017 K [41], the above $E\theta^3$ criteria derived at room temperature ($T \sim 300$ K) should scale with $T/300$ where T is the surface temperature in Kelvin.

When analyzing the overall azimuthal profile, i.e., integrated over the polar direction, we found a general behavior of the azimuthal width σ_ϕ rather similar to that previously observed for the overall polar profile σ_θ [38]. During an E scan where the angle of incidence is fixed, the absolute widths σ_ϕ and σ_θ seem to be remarkably stable for energies $E_\perp$ above a few 100 meV while they increase rapidly for values of $E_\perp$ approaching a few meV (see Fig. 6). During a θ scan, the overall tendency is a linear increase of σ_ϕ and σ_θ for $E_\perp$ above 200 meV and a leveling below this value (Fig. 7). The relative values $\sigma_\phi/2\theta_i$ and $\sigma_\theta/2\theta_i$ in Fig. 8 show the sharp increase below $E_\perp = 200$ meV and a smooth increase above. The ratio of purely elastic diffraction was extracted from the overall azimuthal profile and is interpreted as a measure of the DWF. The derived values in Fig. 7 are found close to, but systematically larger than the ones measured from the polar profiles. Both appear compatible with the specific DWF adapted to GIFAD [7,9,37,41].

The inelastic profile measured on the Laue circle compares with that measured on the overall profile. However, we have a few situations where an accurate determination of the intensities I_m, needed to access the potential energy surface, requires a precise azimuthal line shape. This implies a good description of the inelastic component together with a decent evaluation of the DWF. In addition to the increase of the width, the exact shape was also found to evolve with $E_\perp$, starting from a pure exponential decay (E^*) to a quasi-Gaussian profile, but the $L \cdot G_1^*$ and $L \cdot G_2^*$ suggested in Ref. [7] provides a decent fit both in the quasielastic and quasiclassical regimes as long as elastic diffraction is larger than 1%. The most salient observation presented here is the evolution of the inelastic width

as a function of the distance to the Laue circle suggesting that inelastic diffraction models can be developed from elastic diffraction. By comparing with previous work on the inelastic polar profile, the Sec. VIII suggests that the lateral inelastic profile is more influenced by the surface thermal movement along z and by the location of the turning point z_t than by the in-plane thermal movement. This appears as another specificity of atomic diffraction but remains to be confirmed by more detailed analysis and simulations.

So far the random direction was mainly considered uninteresting. The above investigations strongly suggest that if an accurate line shape is needed for quantitative analysis of diffraction, a reference scattering profile should be recorded along a random direction. The evolution of this profile could probably help to track specific surface defects such as adatoms or terraces, enriching the ability of GIFAD to diagnose the surface quality before, during, and after the growth process [1,3].

As to the limitations, we have indications that the above results are probably not valid for more complex surfaces, for instance, GaAs(001) $\beta_2(2 \times 4)$ [3,33] or Ag(001) [35,60], where deep trenches become visible only along specific directions. For metallic surfaces, soft electronic excitations close to the Fermi level could also contribute to the inelastic signal [61–63].

[1] M. Debiossac, A. Zugarramurdi, H. Khemliche, P. Roncin, A. G. Borisov, A. Momeni, P. Atkinson, M. Eddrief, F. Finocchi, and V. H. Etgens, Combined experimental and theoretical study of fast atom diffraction on the $\beta_2(2 \times 4)$ reconstructed GaAs(001) surface, Phys. Rev. B **90**, 155308 (2014).

[2] S. Lupone, P. Soulisse, and P. Roncin, A large area high resolution imaging detector for fast atom diffraction, Nucl. Instrum. Meth. Phys. Res. B **427**, 95 (2018).

[3] P. Atkinson, M. Eddrief, V. H. Etgens, H. Khemliche, M. Debiossac, A. Momeni, M. Mulier, B. Lalmi, and P. Roncin, Dynamic grazing incidence fast atom diffraction during molecular beam epitaxial growth of GaAs, Appl. Phys. Lett. **105**, 021602 (2014).

[4] M. Debiossac, A. Zugarramurdi, P. Lunca-Popa, A. Momeni, H. Khemliche, A. G. Borisov, and P. Roncin, Transient Quantum Trapping of Fast Atoms at Surfaces, Phys. Rev. Lett. **112**, 023203 (2014).

[5] M. Debiossac and P. Roncin, Image processing for grazing incidence fast atom diffraction, Nucl. Instrum. Meth. Phys. Res. B **382**, 36 (2016).

[6] M. Busch, J. Seifert, E. Meyer, and H. Winter, Evidence for longitudinal coherence in fast atom diffraction, Phys. Rev. B **86**, 241402(R) (2012).

[7] P. Roncin and M. Debiossac, Elastic and inelastic diffraction of fast atoms, Debye-Waller factor, and Mössbauer-Lamb-Dicke regime, Phys. Rev. B **96**, 035415 (2017).

[8] P. Rousseau, H. Khemliche, A. G. Borisov, and P. Roncin, Quantum Scattering of Fast Atoms and Molecules on Surfaces, Phys. Rev. Lett. **98**, 016104 (2007).

[9] P. Rousseau, H. Khemliche, N. Bundaleski, P. Soulisse, A. Momeni, and P. Roncin, Surface analysis with grazing incidence fast atom diffraction (GIFAD), J. Phys.: Conf. Ser. **133**, 012013 (2008).

[10] P. Pan, J. N. Rad, and P. Roncin, A setup for grazing incidence fast atom diffraction, Rev. Sci. Instrum. **93**, 093305 (2022).

[11] C. Henkel, J.-Y. Courtois, and A. Aspect, Atomic diffraction by a thin phase grating, J. Phys. II **4**, 1955 (1994).

[12] M. Debiossac and P. Roncin, Atomic diffraction under oblique incidence: An analytical expression, Phys. Rev. A **90**, 054701 (2014).

[13] A. Zugarramurdi and A. G. Borisov, Transition from fast to slow atom diffraction, Phys. Rev. A **86**, 062903 (2012).

[14] A. Muzas, F. Gatti, F. Martín, and C. Díaz, Diffraction of H from LiF(001): From slow normal incidence to fast grazing incidence, Nucl. Instrum. Meth. Phys. Res. B **382**, 49 (2016).

[15] D. M. Danailov, D. O'Connor, and K. Snowdon, Simulation of ballistic effects during scattering under glancing angles of incidence from crystal surfaces, Surf. Sci. **347**, 215 (1996).

[16] D. Farías, C. Díaz, P. Nieto, A. Salin, and F. Martín, Pronounced out-of-plane diffraction of H_2 molecules from a Pd(111) surface, Chem. Phys. Lett. **390**, 250 (2004).

[17] M. Debiossac, P. Pan, and P. Roncin, Grazing incidence fast atom diffraction, similarities and differences with thermal energy atom scattering (TEAS), Phys. Chem. Chem. Phys. **23**, 7615 (2021).

[18] H. Winter and A. Schüller, Fast atom diffraction during grazing scattering from surfaces, Prog. Surf. Sci. **86**, 169 (2011).

[19] A. Zugarramurdi, M. Debiossac, P. Lunca-Popa, L. S. Alarcón, A. Momeni, H. Khemliche, P. Roncin, and A. G. Borisov, Surface-grating deflection of fast atom beams, Phys. Rev. A **88**, 012904 (2013).

[20] P. Roncin, M. Debiossac, H. Oueslati, and F. Raouafi, Energy loss and inelastic diffraction of fast atoms at grazing incidence, Nucl. Instrum. Meth. Phys. Res. B **427**, 100 (2018).

[21] F. Aigner, N. Simonović, B. Solleder, L. Wirtz, and J. Burgdörfer, Suppression of Decoherence in Fast-Atom Diffraction at Surfaces, Phys. Rev. Lett. **101**, 253201 (2008).

[22] A. Sanz and S. Miret-Artés, A trajectory-based understanding of quantum interference, J. Phys. A: Math. Theor. **41**, 435303 (2008).

[23] C. Brand, M. Debiossac, T. Susi, F. Aguillon, J. Kotakoski, P. Roncin, and M. Arndt, Coherent diffraction of hydrogen through the 246 pm lattice of graphene, New J. Phys. **21**, 033004 (2019).

[24] D. Danailov, K. Gärtner, and A. Caro, Computer simulation of the reflection of energetic ions from crystal surfaces at glancing incidence, Nucl. Instrum. Meth. Phys. Res. B **153**, 191 (1999).

[25] D. M. Danailov, Angular spectra of rainbow scattering at glancing keV He^+ bombardment of NiAl(100) surface with transverse energies in the range 1 to 10eV, Nucl. Instrum. Meth. Phys. Res. B **264**, 29 (2007).

[26] J. Connor and W. Jakubetz, Rainbow scattering in atomic collisions: A regge pole analysis, Mol. Phys. **35**, 949 (1978).

[27] A. Schüller and H. Winter, Supernumerary Rainbows in the Angular Distribution of Scattered Projectiles for Grazing Collisions of Fast Atoms with a LiF(001) Surface, Phys. Rev. Lett. **100**, 097602 (2008).

[28] M. Gravielle, A. Schüller, H. Winter, and J. Miraglia, Fast atom diffraction for grazing scattering of Ne atoms from a LiF(001) surface, Nucl. Instrum. Meth. Phys. Res. B **269**, 1208 (2011).

[29] M. S. Gravielle and J. E. Miraglia, Semiquantum approach for fast atom diffraction: Solving the rainbow divergence, Phys. Rev. A **90**, 052718 (2014).

[30] J. S. Briggs, Trajectories and the perception of classical motion in the free propagation of wave packets, Nat. Sci. **2**, e20210089 (2022).

[31] E. Pollak and S. Miret-Artés, Second-order semiclassical perturbation theory for diffractive scattering from a surface, J. Phys. Chem. C **119**, 14532 (2015).

[32] W. Allison, S. Miret-Artés, and E. Pollak, Perturbation theory of scattering for grazing-incidence fast-atom diffraction, Phys. Chem. Chem. Phys. **24**, 15851 (2022).

[33] M. Debiossac, P. Atkinson, A. Zugarramurdi, M. Eddrief, F. Finocchi, V. Etgens, A. Momeni, H. Khemliche, A. Borisov, and P. Roncin, Fast atom diffraction inside a molecular beam epitaxy chamber, a rich combination, Appl. Surf. Sci. **391**, 53 (2017).

[34] B. Lalmi, H. Khemliche, A. Momeni, P. Soulisse, and P. Roncin, High resolution imaging of superficial mosaicity in single crystals using grazing incidence fast atom diffraction, J. Phys.: Condens. Matter **24**, 442002 (2012).

[35] C. A. Rios Rubiano, G. A. Bocan, M. S. Gravielle, N. Bundaleski, H. Khemliche, and P. Roncin, *Ab* initio potential for the He-Ag(110) interaction investigated using grazing-incidence fast-atom diffraction, Phys. Rev. A **87**, 012903 (2013).

[36] J. Seifert, J. Lienemann, A. Schüller, and H. Winter, Studies on coherence and decoherence in fast atom diffraction, Nucl. Instrum. Meth. Phys. Res. B **350**, 99 (2015).

[37] J. R. Manson, H. Khemliche, and P. Roncin, Theory of grazing incidence diffraction of fast atoms and molecules from surfaces, Phys. Rev. B **78**, 155408 (2008).

[38] P. Pan, M. Debiossac, and P. Roncin, Polar inelastic profiles in fast-atom diffraction at surfaces, Phys. Rev. B **104**, 165415 (2021).

[39] J. Villette, A. G. Borisov, H. Khemliche, A. Momeni, and P. Roncin, Subsurface-Channeling-Like Energy Loss Structure of the Skipping Motion on an Ionic Crystal, Phys. Rev. Lett. **85**, 3137 (2000).

[40] J. Villette, Ph.D. thesis, Université Paris sud-XI, 2000, https://theses.hal.science/tel-00106816/file/These.J.Villette.pdf.

[41] P. Pan, M. Debiossac, and P. Roncin, Temperature dependence in fast-atom diffraction at surfaces, Phys. Chem. Chem. Phys. **24**, 12319 (2022).

[42] K. H. Rieder and N. Garcia, Energy Dependence and Softness of the Potential for He Scattering from Ni(110), Phys. Rev. Lett. **49**, 43 (1982).

[43] N. Kalashnyk, H. Khemliche, and P. Roncin, Atom beam triangulation of organic layers at 100 mev normal energy: Self-assembled perylene on Ag(110) at room temperature, Appl. Surf. Sci. **364**, 235 (2016).

[44] M. Debiossac, P. Roncin, and A. G. Borisov, Refraction of fast Ne atoms in the attractive well of a LiF(001) surface, J. Phys. Chem. Lett. **11**, 4564 (2020).

[45] A. Tamtögl, M. Mayrhofer-Reinhartshuber, N. Balak, W. Ernst, and K.-H. Rieder, Elastic and inelastic scattering of he atoms from Bi(111), J. Phys.: Condens. Matter **22**, 304019 (2010).

[46] G. Anemone, A. A. Taleb, G. Benedek, A. Castellanos-Gomez, and D. Farías, Electron–phonon coupling constant of 2H-MoS₂ (0001) from helium-atom scattering, J. Phys. Chem. C **123**, 3682 (2019).

[47] G. Benedek, S. Miret-Artés, J. Manson, A. Ruckhofer, W. E. Ernst, and A. Tamtogl, Origin of the electron–phonon interaction of topological semimetal surfaces measured with helium atom scattering, J. Phys. Chem. Lett. **11**, 1927 (2020).

[48] G. Benedek, M. Bernasconi, D. Campi, I. V. Silkin, I. Chernov, V. M. Silkin, E. V. Chulkov, P. M. Echenique, J. P. Toennies, G. Anemone *et al.*, Evidence for a spin acoustic surface plasmon from inelastic atom scattering, Sci. Rep. **11**, 1506 (2021).

[49] M. C. Schram and E. J. Heller, Approach to coherent interference fringes in helium-surface scattering, Phys. Rev. A **98**, 022137 (2018).

[50] M. C. Schram and E. J. Heller, Hitting a ball on a spring: A simple model for understanding decoherence with wavefunctions, Eur. J. Phys. **41**, 025401 (2020).

[51] A. Schüller, S. Wethekam, D. Blauth, H. Winter, F. Aigner, N. Simonović, B. Solleder, J. Burgdörfer, and L. Wirtz, Rumpling of LiF(001) surface from fast atom diffraction, Phys. Rev. A **82**, 062902 (2010).

[52] L. Frisco and M. S. Gravielle, Phonon contribution in grazing-incidence fast atom diffraction from insulator surfaces, Phys. Rev. A **100**, 062703 (2019).

[53] L. Frisco and M. S. Gravielle, Thermal effects on helium scattering from LiF (001) at grazing incidence, Phys. Rev. A **102**, 062821 (2020).

[54] L. Frisco and M. Gravielle, Decoherent phonon effects in fast atom-surface scattering, Nucl. Instrum. Meth. Phys. Res. B **540**, 1 (2023).

[55] Y. Ekinci and J. Toennies, Thermal expansion of the LiF(001) surface, Surf. Sci. **563**, 127 (2004).

[56] J. L. Beeby, The scattering of helium atoms from surfaces, J. Phys. C: Solid State Phys. **4**, L359 (1971).

[57] D. Farías and K. Rieder, Atomic beam diffraction from solid surfaces, Rep. Prog. Phys. **61**, 1575 (1998).

[58] M. Debiossac, A. Zugarramurdi, Z. Mu, P. Lunca-Popa, A. J. Mayne, and P. Roncin, Helium diffraction on SiC grown graphene: Qualitative and quantitative descriptions with the hard-corrugated-wall model, Phys. Rev. B **94**, 205403 (2016).

[59] A. P. Jardine, S. Dworski, P. Fouquet, G. Alexandrowicz, D. J. Riley, G. Y. H. Lee, J. Ellis, and W. Allison, Ultrahigh-resolution spin-echo measurement of surface potential energy landscapes, Science **304**, 1790 (2004).

[60] N. Bundaleski, H. Khemliche, P. Soulisse, and P. Roncin, Grazing Incidence Diffraction of keV Helium Atoms on a Ag(110) Surface, Phys. Rev. Lett. **101**, 177601 (2008).

[61] H. Khemliche, N. Bundaleski, P. Soulisse, and P. Roncin, Electron excitations in grazing diffraction of fast He on a Ag(110) surface. A tribute to Hannspeter Winter, Nucl. Instrum. Meth. Phys. Res. B **267**, 620 (2009).

[62] M. Busch, A. Schüller, S. Wethekam, and H. Winter, Fast atom diffraction at metal surface, Surf. Sci. **603**, L23 (2009).

[63] N. Bundaleski, P. Soulisse, A. Momeni, H. Khemliche, and P. Roncin, Decoherence in fast atom diffraction from surfaces, Nucl. Instrum. Meth. Phys. Res. B **269**, 1216 (2011).